MATERIALS SCIENCE

Soft nanoforest of metal single atoms for free diffusion catalysis

Yan Sun[1]†, Yipeng Zang[2]†, Bowen He[3]†, Geyu Lin[1], Zhengwu Liu[4], Lei Yang[1], Liwei Chen[3], Lina Li[4]*, Xi Liu[3]*, Chengshuo Shen[5]*, Huibin Qiu[1]*

Copyright © 2025 The Authors, some rights reserved; exclusive licensee American Association for the Advancement of Science. No claim to original U.S. Government Works. Distributed under a Creative Commons Attribution NonCommercial License 4.0 (CC BY-NC).

Metal single atoms are of increasing importance in catalytic reactions. However, the mass diffusion is yet substantially limited by the confined surface of the support in comparison to homogeneous catalysis. Here, we demonstrate that cylindrical micellar brushes with highly solvated poly(2-vinylpyridine) coronas can immobilize 33 types of metal single atoms with 8.3 to 40.9 weight % contents on conventional electrodes under ambient conditions. This is favored by the forest-like hierarchically open soft structure of the micellar brushes and the dynamic coordination between the metals and the pyridine groups. It was found that the nanoforests of individual noble metal single atoms can be well solvated in an aqueous electrolyte to comprehensively expose the atomic active sites and the nanoforest of Pt single atoms on nickel foam reveals high electrochemical performance for hydrogen evolution. The micellar brush support also enables the simultaneous anchoring of multiple single atoms on the cathode of an anion-exchange membrane electrolyzer for long-term stable water electrolysis.

INTRODUCTION

Heterogeneous catalysts with excellent stability and recyclability have been widely used in industrial chemical catalysis and electrochemical reactions. However, their complex and inhomogeneous structure critically hinders the association between the reaction substrate and the catalytically active sites, thereby limiting the catalytic activity (*1*). This is in marked contrast with the homogeneous catalysts that have uniform active centers, sufficient contact of the catalyst and substrate, and well-defined coordination environments (*2*, *3*). Recently, single-atom (SA) catalysts have emerged as a bridge to connect heterogeneous and homogeneous catalysis, which offer high atom utilization efficiency, prominent stability, and easy separation capability (*4*–*9*). These features have stimulated the emergence of a rich variety of synthesis strategies for SA catalysts (*10*–*13*). Generally, SAs are dispersed/anchored on solid supports after surface engineering treatment via strong interactions, which prevent the aggregation of isolated atoms. The coordination sites (e.g., O, N and S) on metal oxides/nitrides/dichalcogenides/carbon-derived matrixes or porous framework have been widely used to immobilize SAs (*14*–*21*). The formation of stabilized SAs normally involves a sintering process, which frequently results in an irregular distribution of SAs and in some instance causes a severe coverage of SAs by the collapsed matrix, thus limiting the exposure of homogeneous atomic active sites (*22*). Such harsh conditions also impair the practical application of SA catalysts. Moreover, most supports are insolvable in a reaction environment, which hampers the diffusion of reaction media to the active sites and consequently render a low atomic catalytic activity. Therefore, it is highly desirable to develop a solvable support for SA catalysts, aiming at more homogeneous-like free diffusion catalysis.

Here, we develop a soft nanoforest system derived from micellar brush of block copolymers (*23*–*25*) to modify the surface of conventional electrodes for the immobilization of SAs, simply by immersing in the solutions of corresponding metal ion precursors at room temperature. The abundant and highly solvated pyridine groups in the corona of the micellar brush provide feasible coordinative sites for the capture of metal ions, which allows the further formation of a wide category of SA catalysts at an ultrahigh loading level (up to 40.9 wt %). The forest-like environment also allows the simultaneous immobilization of multiple SAs. As a result of the well-solvated structure, open diffusion pathway, exposed atomic active sites, ultrahigh content, orbital flexibility, dynamic coordination, and synergetic effects, the nanoforests of SAs reveal high catalytic activity on electrochemical hydrogen evolution, anion-exchange membrane (AEM) electrolyzer, and CO_2 electroreduction.

RESULTS

Fabrication of the metal SA nanoforest

Nickel foam was selected as a conductive substrate to grow micellar brushes of poly(ferrocenyldimethylsilane)-*b*-poly(2-vinylpyridine) (PFS-*b*-P2VP) (figs. S1 and S2) via living crystallization-driven self-assembly according to our previous work (*23*). Notably, the resulting micellar brush presented an erect structure in the solution, poised to the immobilization of further added species (fig. S3). Subsequently, the micellar brush–coated nickel foam was immersed in a solution of Na_2PtCl_4 in 1:1 (v/v) water/isopropanol. The highly solvated P2VP coronas of the micellar brush with extremely concentrated pyridine groups would efficiently capture the $PtCl_4^{2-}$ ions through electrostatic interactions in the initial stage (Fig. 1, top and middle). Subsequently, the pyridine groups gradually replace the Cl^- ligands through coordination interactions, yielding a stable polymeric coordination composite (Fig. 1, bottom). The forest-like hierarchically open structure of the micellar brushes meanwhile offers sufficient

[1]School of Chemistry and Chemical Engineering, Zhangjiang Institute for Advanced Study, Frontiers Science Center for Transformative Molecules, State Key Laboratory of Metal Matrix Composites, Shanghai Jiao Tong University, Shanghai 200240, P. R. China. [2]State Key Laboratory of Catalysis, Dalian National Laboratory for Clean Energy, Dalian Institute of Chemical Physics, Chinese Academy of Sciences, Dalian 116023, P. R. China. [3]In situ Centre for Physical Sciences, Frontiers Science Center for Transformative Molecules, School of Chemistry and Chemical Engineering, Shanghai Jiao Tong University, Shanghai 200240, P. R. China. [4]Shanghai Synchrotron Radiation Facility, Shanghai Advanced Research Institute, Shanghai 201204, P. R. China. [5]School of Chemistry and Chemical Engineering, Zhejiang Sci-Tech University, Xiasha Campus, Hangzhou 310018, P. R. China.
*Corresponding author. Email: lilina@sinap.ac.cn (L.L.); liuxi@sjtu.edu.cn (X.L.); shenchengshuo@zstu.edu.cn (C.S.); hbqiu@sjtu.edu.cn (H.Q.)
†These authors contributed equally to this work.

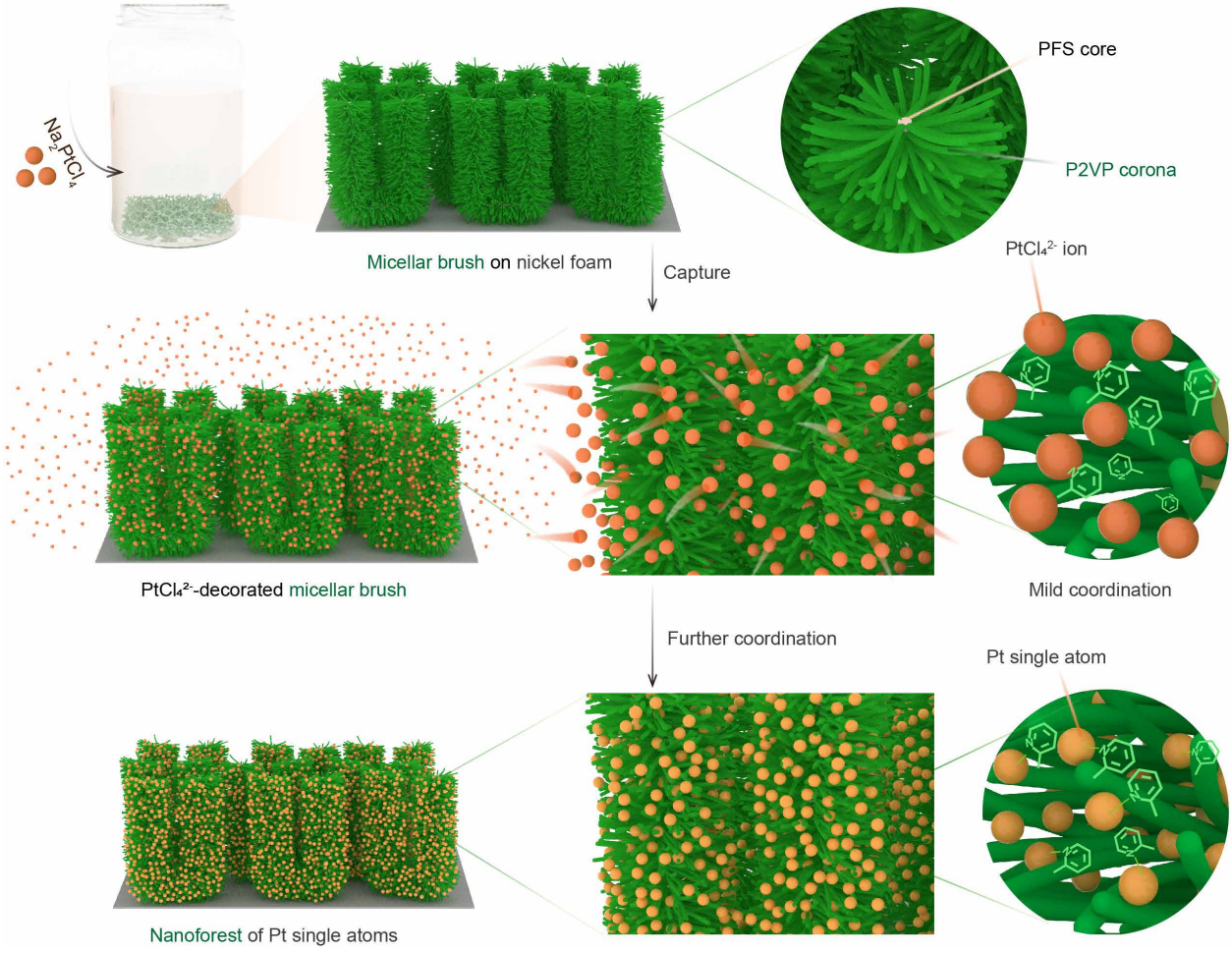

Fig. 1. Fabrication of the Pt SA nanoforest. Schematic illustration of the fabrication process of the Pt SA nanoforest through mild coordination.

space and anchor sites for the immobilization of abundant metal ions in an SA form.

While the pristine PFS-*b*-P2VP micellar brush revealed a collapsed morphology after drying (figs. S4 and S5), the Pt-decorated micellar brush appeared to be fairly erect and uniformly distributed on the nickel foam (Fig. 2A and fig. S6). High-angle annular dark-field scanning transmission electron microscopy (HAADF-STEM) image and corresponding element mapping revealed a homogeneous distribution of N and Pt elements in the micellar brush (Fig. 2B). Aberration-corrected annular dark-field STEM (AC-ADF-STEM) images showed that the Pt atoms were atomically dispersed in the micellar brush, without any detectable existence of clusters or agglomerates (Fig. 2C and fig. S7). The bright spots were ~0.17 nm in diameter, corresponding to the theoretical size of a single Pt atom (fig. S8). Inductively coupled plasma mass spectrometry (ICP-MS) analysis revealed a large Pt loading of 28.4 wt % (fig. S9), which is higher than most previously reported Pt SA–based materials (table S1) (*7*, *26*–*38*). Energy-dispersive spectrometric (EDS) mapping and x-ray photoelectron spectroscopy (XPS) measurements further confirmed the existence of a high content of Pt SA (32.30 and 26.59 wt %, respectively). It was apparent that the PFS-*b*-P2VP micellar brush favors the formation of Pt SAs in a highly concentrated manner, yielding a soft nanoforest of SAs.

To track the formation of Pt SAs in the micellar brush, we monitored the evolution of the metal species and the pyridine anchor sites during the immersion process. XPS spectra of Pt 4f showed that the valence of Pt remained constant at +2, whereas the peak gradually shifted to a lower binding energy region (fig. S10C), indicating an interaction with the pyridine groups. High-resolution XPS spectra of N 1s showed that the signal at 398.6 eV (pyridinic N) continuously decreased with the emergence of an additional signal at 399.5 eV (Fig. 2D), which can be attributed to the formation of the N-Pt bond. Notably, the ratio of N-Pt bonding increased to ca. 66% after immersion for more than 30 min, indicating an intensive coordination with Pt SAs (Fig. 2D and fig. S10, A and B). Only a negligible amount of Cl was detected in the final composite (fig. S10D) and hence the Cl^- ligands were almost completely replaced by the pyridine groups. Fourier-transformed extended x-ray absorption fine structure (FT-EXAFS) spectra of the composite showed a main peak at ~1.57 Å (Fig. 2E), which can be attributed to N-coordinated Pt SAs (*39*). No evidence of Pt-Pt scattering path was observed compared to Pt foil, indicating that the Pt elements were atomically decorated in the micellar brush. Fitting of EXAFS spectrum (Fig. 2E, fig. S11, and table S2) suggested that each Pt SA coordinated with 3.7 pyridine groups on average, forming a stable coordinating complex. Roughly, 57%

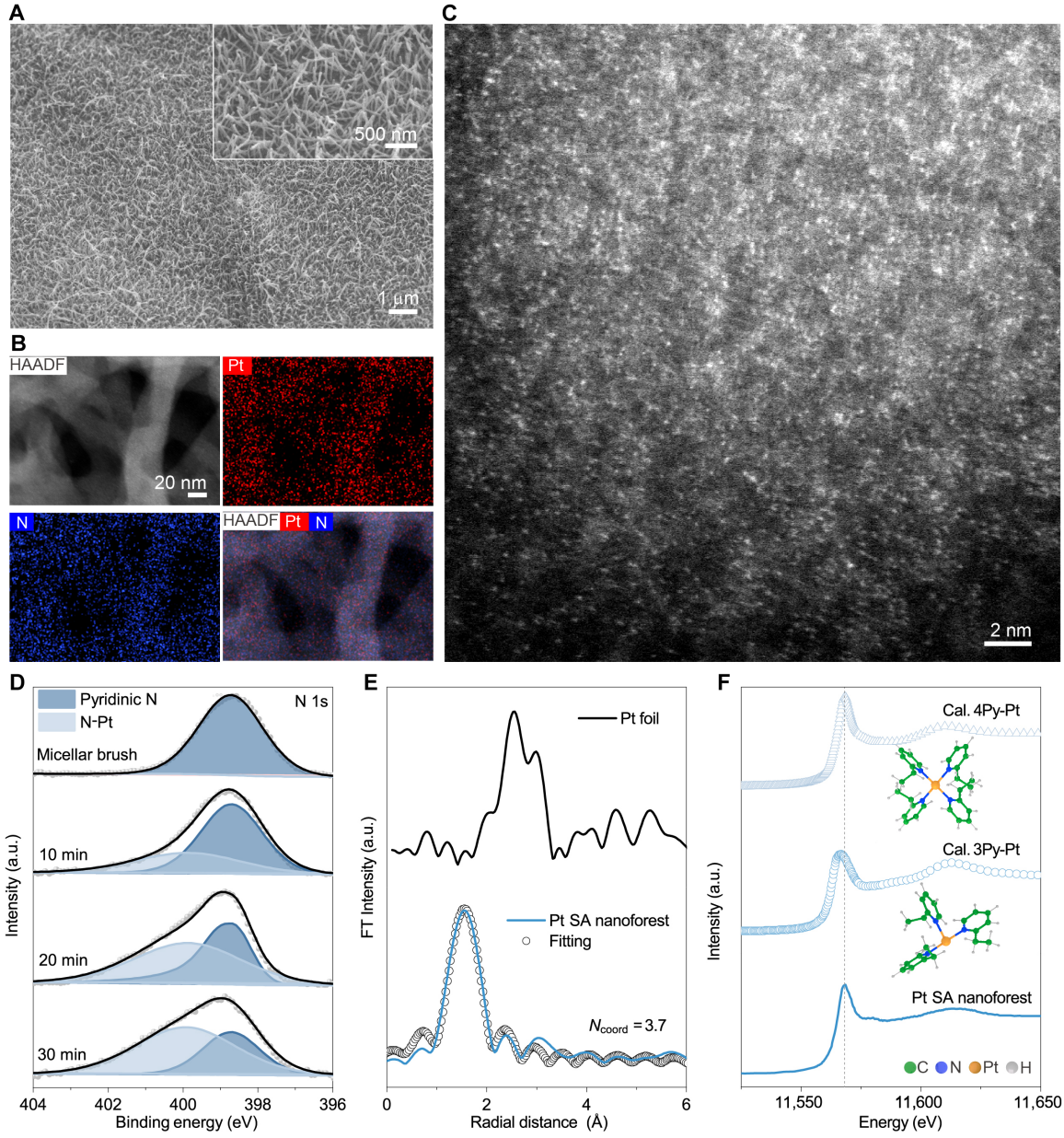

Fig. 2. Analysis of the Pt SA nanoforest. (**A**) Scanning electron microscopy (SEM) image of the Pt SA nanoforest. (**B**) HAADF-STEM image and corresponding element mapping of the Pt SA nanoforest, where blue represents the N element and red identifies the Pt element. (**C**) AC-ADF-STEM images of the Pt SA nanoforest. (**D**) XPS spectra of N 1s for the samples obtained at different immersion times. (**E**) FT-EXAFS spectra of the Pt foil and Pt SA nanoforest, and the corresponding EXAFS fitting curve of the Pt SA nanoforest for *R*-space. N_{coord} denotes the average number of ligands coordinated with a Pt atom. (**F**) Experimental Pt L_3-edge XANES spectra of the Pt SA nanoforest and calculated XANES data for the configurations in which an Pt atom is coordinated with three or four pyridine groups. Py represents the 2-thylpyridine group.

of the pyridine groups were used to coordinate with the Pt atoms, which was approximate to the value estimated by the XPS spectra of N 1s. Theoretical x-ray absorption near-edge structure (XANES) spectrum simulation further showed that the 4Py-Pt (four pyridine groups surrounding one Pt atom) model is in better agreement with the experimental data than the 3Py-Pt configuration (Fig. 2F).

To certify the generality of the micellar brush–derived SA nanoforest, we explored another 32 types of metal elements, including transition, post transition, lanthanide, alkali, and alkaline earth metals. AC-ADF-STEM images showed that all these metals were successfully decorated and atomically dispersed in the micellar brush (Fig. 3A, panels A and C of figs. S12 to S43, and fig. S44). HAADF-STEM and corresponding element mappings confirmed the uniform dispersion of N and metals in the micellar brush (panel B of figs. S12 to S43). ICP-MS showed high atomic loadings (8.3 to 40.9 wt %) for these 32 types of SAs (Fig. 3B). XPS spectra showed that these SAs were in positive valance states, with no metallic signal detected, indicating the absence of metal clusters or nanoparticles (NPs; panel D of figs. S12 to S43). XPS spectra of N 1s confirmed the association between the metal and nitrogen atoms, except the alkali and alkaline earth metals (panel E of figs. S12 to

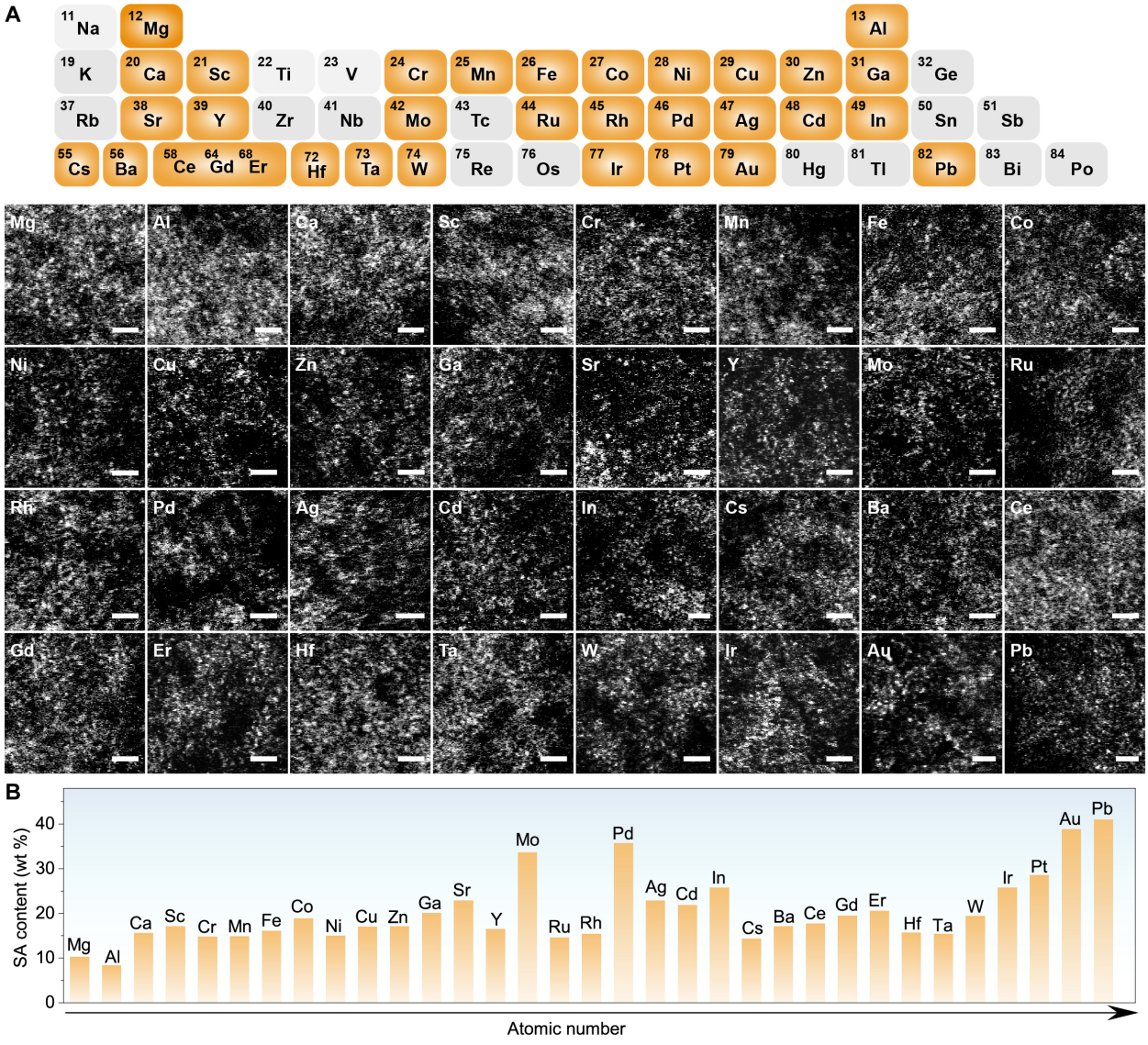

Fig. 3. Scope of metal SA nanoforests. (**A**) AC-ADF-STEM images of 32 metal SA nanoforests. Scale bars represent 1 nm. (**B**) Metal loadings determined by ICP-MS (Ni loading determined by XPS) in the above nanoforest.

S43). Taking the Ag SA nanoforest as an example, FT-EXAFS spectra showed a major peak at ~1.58 Å (fig. S30G), which can be ascribed to the N-Ag coordination (*40*). No Ag-Ag interaction was observed compared to Ag foil, indicating that the Ag atoms were atomically decorated in the micellar brush. Fitting EXAFS spectrum revealed that each Ag SA coordinated with 2.2 pyridine groups on average (table S4). FT-EXAFS spectra of Mn, Fe, Co, Ni, Cu, Zn, Ru, Pd, Ir, and Au SA nanoforests also showed that the SAs were decorated in the micellar brush and coordinated with the pyridine groups (figs. S17 to S22, S27, S29, S41, and S42). Regarding the alkali and alkaline metals, no coordination was found between the metal and N atoms (*27*), and they were probably immobilized through cation-π interactions (*41*).

Formation mechanism of the metal SA nanoforest

Density functional theory (DFT) calculations were further conducted to study the formation mechanism of the metal SA nanoforest. 2-Ethylpyridine was used to represent the pyridyl polymer P2VP for simplicity in the calculation. For the formation of the Pt SA nanoforest, the micellar brush first associates with the $PtCl_4^{2-}$ ion by forming a pyridine-Pt coordination bond and one Cl^- is released with a decrease of free energy of 5.7 kcal mol^{-1} (Fig. 4A). Subsequently, the second pyridine group substitutes at the *trans* position of the $PtCl_3Py^-$ intermediate with a decrease of free energy of 5.8 kcal mol^{-1} (for *cis*-isomer, the decrease of free energy is only 2.3 kcal mol^{-1}, fig. S45A). The third substitution of a Cl^- by a pyridine group shows no change in free energy. However, the fourth substitution leads to a further release of free energy by 2.4 kcal mol^{-1}, yielding a fairly stable coordination complex. When the Pt atoms are not completely saturated in coordination, the formation of the Pt-Pt bond requires overcoming a high energy barrier of 85.9 kcal mol^{-1}, indicating difficulty in the formation of metal clusters or NPs (fig. S46). The substitution process of $PdCl_4^{2-}$ follows a similar pathway to $PtCl_4^{2-}$ and

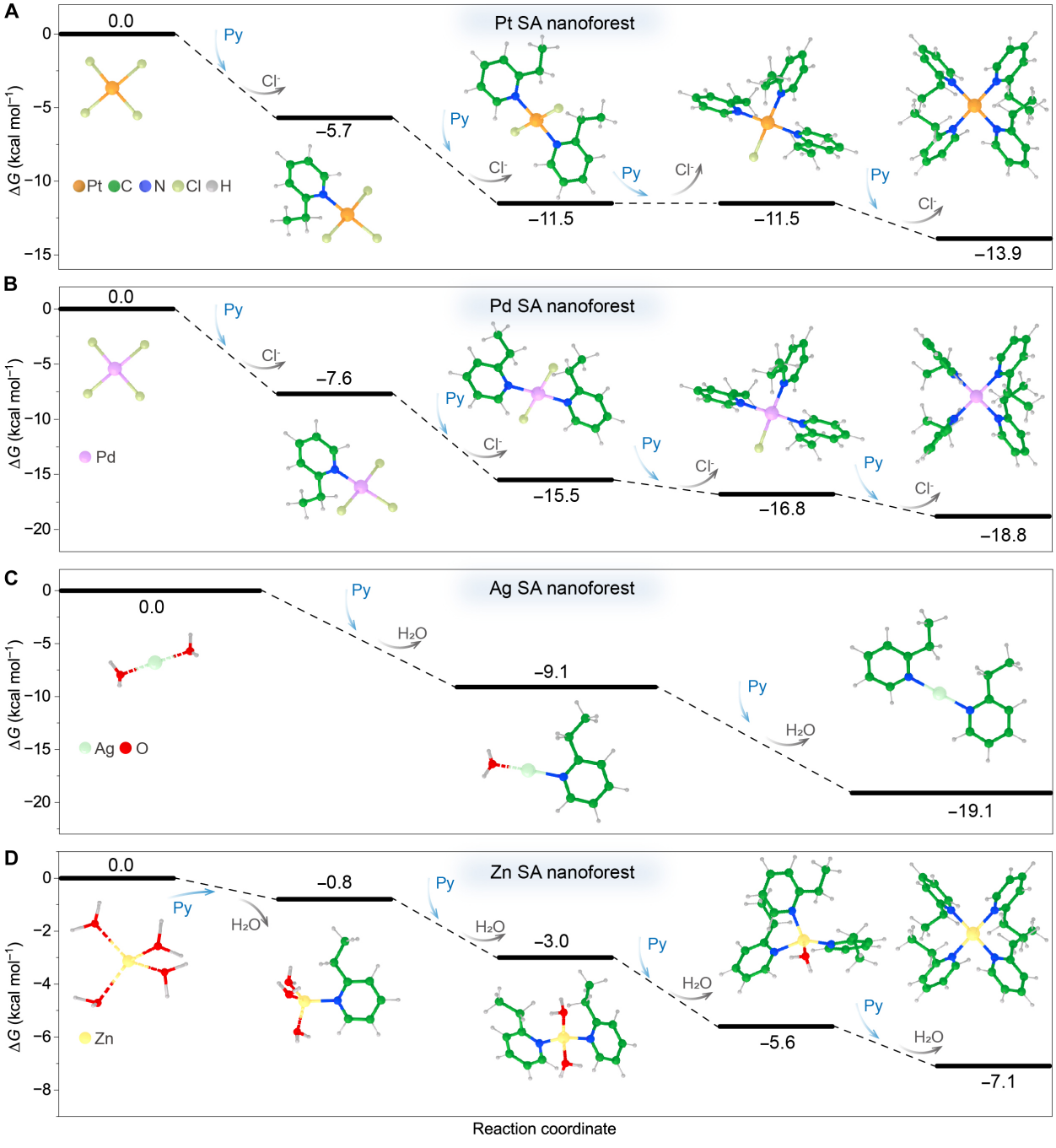

Fig. 4. Formation mechanism of the metal SA nanoforest. DFT calculation of the energy pathway and possible intermediates for the formation of (**A**) Pt, (**B**) Pd, (**C**) Ag, and (**D**) Zn SA nanoforests.

eventually leads to a total release of free energy by 18.8 kcal mol^{-1} (Fig. 4B and fig. S45B). For Ag^+ and Zn^{2+}, considering that the metal precursors were $AgNO_3$ and $Zn(NO_3)_2$, respectively, hydrated cations were used for the calculation (Fig. 4, C and D). The substitution by the pyridyl groups also reveals a sequential decrease in free energy. For Ag^+, the most stable complex is found to be $AgPy_2^+$, while for Zn^{2+}, the final complex is calculated to be $ZnPy_4^{2+}$. Obviously, the abundant pyridine groups in the micellar brush play an important role in anchoring and stabilizing the diverse SAs.

Catalytic performance

To explore the utilization of these SAs in catalysis, representatively, we evaluated the performance of the Pt SA nanoforest in electrocatalytic hydrogen evolution reaction (HER) in an aqueous solution of KOH (1.0 M). As shown by the fluid atomic force microscopy (AFM) image (Fig. 5A), the Pt SA nanoforest revealed an erect structure in the electrolyte as only their top can be observed. After immersing the Pt SA nanoforest in KOH for 24 hours, the main peak in the FT-EXAFS spectra shifted to 1.68 Å and the fitting result

revealed that each Pt atom coordinated with 3.1 pyridine groups and 1.1 hydroxyl groups on average (Fig. 5B, fig. S47, and table S5), indicating the dynamic coordination between a Pt atom and the surrounding pyridine groups. The calculated XANES spectrum confirmed the 3Py-Pt-OH model (inset of fig. S47B). Besides, theoretical results further revealed that $[3Py\text{-}Pt\text{-}OH]^+$ is more stable than $[4Py\text{-}Pt]^{2+}$ under basic conditions (pH 14, fig. S48).

Compared to the nickel foams decorated with pristine micellar brush (346.5 mV at 100 mA cm^{-2}, 123 mV dec^{-1}, 88.62 ohms), Pt NPs on nickel foam (fig. S49, 262.7 mV at 100 mA cm^{-2}, 80 mV dec^{-1}, 57.93 ohms), 20 wt % Pt/C on nickel foam (104.9 mV at 100 mA cm^{-2}, 43 mV dec^{-1}), and also the pristine nickel foam (370.1 mV at 100 mA cm^{-2}, 124 mV dec^{-1}, 100.43 ohms), the Pt SA nanoforest–decorated nickel foam showed considerably lower overpotential (76.1 mV at 100 mA cm^{-2}), Tafel slope (38 mV dec^{-1}), charge-transfer resistance (R_{ct}, 8.01 ohms) (Fig. 5C and fig. S52, A and B). The mass current density of the Pt SA nanoforest–decorated nickel foam reached 25.9 A mg_{Pt}^{-1} at an overpotential of 50 mV (Fig. 5D), which was remarkably higher than that of the Pt NP (0.31 A mg_{Pt}^{-1})–decorated, 20 wt % Pt/C–decorated nickel foams (0.87 A mg_{Pt}^{-1}), and the most previously reported Pt-based materials (table S7) (*28*, *29*, *31*–*33*, *35*–*37*, *42*–*57*). Such improved HER performance can be attributed to the ultrahigh loading of Pt SAs and modulated electronic structure, as well as the forest-like erect and hierarchically open structure, which enhanced the utilization efficiency of SAs (Fig. 5E and fig. S53). In addition, the Pt SA nanoforest showed no notable decay after testing for 500 hours at −0.92 V versus RHE targeting at a current density of 100 mA cm^{-2} (Fig. 5F). Notably, the Pt SA nanoforest with a lower Pt content (10.7 wt %) that obtained at a lower feeding amount of Na_2PtCl_4 (figs. S50 and S51) revealed a considerably increased overpotential of 106.2 mV at a current density of 100 mA cm^{-2} (Fig. 5C) and a decreased mass current density of 18.6 A mg_{Pt}^{-1}. On the other hand, overfeeding of the Na_2PtCl_4 precursor led to the formation of clusters (42.7 wt % Pt) and NPs (96.4 wt % Pt) (figs. S50 and S51), which revealed smaller overpotentials of 70.9 and 67.9 mV, respectively, at a current density of 100 mA cm^{-2} (Fig. 5C). However, the mass current density decreased to 22.6 and 10.3 A mg_{Pt}^{-1}, respectively. Besides, the electrocatalyst surface area (ECSA) and H_2 turnover frequency (TOF) value of the Pt SA nanoforest (28.4 wt % Pt) was calculated to be 261.9 m^2 g_{pt}^{-1} and 18.7 s^{-1}, respectively, considerably higher than the Pt cluster–decorated micellar brush (42.7 wt % Pt, 238.9 m^2 g_{pt}^{-1}, 17.9 s^{-1}), the Pt NP–decorated micellar brush (96.4 wt % Pt, 189.6 m^2 g_{pt}^{-1}, 10.2 s^{-1}), Pt NPs on nickel foam (7.9 m^2 g_{pt}^{-1}, 7.3 s^{-1}), 20 wt % Pt/C on nickel foam (17.3 m^2 g_{pt}^{-1}, 8.2 s^{-1}, fig. S52, C to E), and most previously reported Pt-based materials (table S7). After the HER test for 500 hours, the nanoforest retained well on the nickel foam and the Pt SAs remained uniformly dispersed in the micellar brush (fig. S54), although the loading of Pt SA was slightly decreased to 25.5 wt %. FT-EXAFS spectra confirmed the retaining of the N/OH-coordinated Pt SAs (fig. S55 and table S8), indicating a high stability of the SAs in the soft micellar brush.

DFT calculations further provide deeper insights into the HER catalyzed by the metal SA nanoforest system (Fig. 5G and fig. S56B). Starting from the $[3Py\text{-}Pt\text{-}OH]^+$ complex, one hydroxyl group was exchanged by water molecular with the free energy increased by 24.6 kcal mol^{-1}. Then, one pyridine group is released and one electron is accepted, and the free energy is reduced by 20.0 kcal mol^{-1}. Subsequently, water dissociation occurs on the $[2Py\text{-}Pt\text{-}H_2O]^+$ complex with an increase of free energy of 8.6 kcal mol^{-1}. Notably, the direct dissociation of water from the $[3Py\text{-}Pt\text{-}H_2O]^{2+}$ complex involves a large increase of free energy of +37.0 kcal mol^{-1} (fig. S56A). Next, the Pt complex releases one hydroxyl anion and receives one electron, with the free energy remarkably reduced by 41.2 kcal mol^{-1}. Afterward, another water molecule coordinates with the Pt complex and the free energy is further decreased by 20.6 kcal mol^{-1}. The subsequent water dissociation process results in an increase in free energy of 20.4 kcal mol^{-1}, with two hydrogen atoms and one hydroxyl anion coordinating directly to the Pt center. Subsequently, one pyridine group is received and the free energy is increased by 17.6 kcal mol^{-1}. This is followed by the release of one hydroxyl anion, with the free energy decreased by 4.1 kcal mol^{-1}. The overall increase of free energy in the above two steps is considerably lower than the direct release of a hydroxyl anion from the $[2Py\text{-}Pt\text{-}OH\text{-}2H]^{2+}$ complex (58.2 kcal mol^{-1}). Last, by releasing a H_2 molecule and receiving one hydroxyl group, the original complex recovered along with a release of free energy of 36.9 kcal mol^{-1}. It appears that the pyridine-Pt coordination in the nanoforest is rather reversible and dynamic, which favors the adsorption and further dissociation of water molecule, as well as the release of hydroxyl anion, and thus promotes the evolution of H_2.

It was found that the nickel foam decorated with the Pt SA nanoforest possessed high hydrophilicity (static-water-droplet contact angle = 26°) and aerophobicity (air-bubble contact angle = 150°). Thus, small hydrogen bubbles were quickly released from the electrode (fig. S58), which further promoted the HER. We also prepared Au and Ag SA nanoforest–decorated graphene oxide composites (fig. S59) and evaluated their activity toward electroreduction of CO_2. The two nanoforests both exhibited high Faradaic efficiency of more than 90% and high partial current density (383 mA cm^{-2} at −1.31 V for the Ag SA nanoforest and 221 mA cm^{-2} at −1.0 V for the Au SA nanoforest) for the conversion of CO_2 to C_1 products (figs. S60 and S61 and tables S9 and S10) (*58*–*66*).

Multimetallic SA nanoforest

Compared to individual SAs, multimetallic SAs offer more diverse electronic structures and synergistic active centers (*67*, *68*). However, the synthesis of multimetallic SA catalysts was critically restricted by the distinct features of various metals and the propensity to aggregate during the preparation process (*69*). To address this challenge, we used the micellar brush with forest-like hierarchically open structure and abundant pyridine anchor sites to fabricate nanoforests containing two (Pt-Pd, Pt-Ir, Pt-Au, Pt-Ag, and Ir-Ru), five (Co-Cu-Zn-Pt-Ir), and even eight types (Fe-Co-Ni-Cu-Zn-Pt-Pd-Ir) of metals (Fig. 6 and figs. S62 to S67). Regarding the Pt-Ir SA nanoforest, AC-ADF-STEM images showed that the metal SAs were atomically dispersed in the micellar brush (Fig. 6A and fig. S65), and the Pt and Ir content was estimated to be 12.3 and 8.2 wt % according to ICP-MS. Element mapping further confirmed the uniform dispersion of Pt and Ir SAs (Fig. 6B). FT-EXAFS spectra of Pt and Ir SAs showed major peaks at ~1.54 and ~1.80 Å (Fig. 6C and fig. S66), respectively, again corresponding to atomically dispersed Pt and Ir. The nanoforest of eight metals (Fe-Co-Ni-Cu-Zn-Pt-Pd-Ir) also revealed atomically and uniform dispersed metal SAs (Fig. 6, D and E, and fig. S69). FT-EXAFS spectra of the eight metals all showed a major peak corresponding to the SAs (Fig. 6F and fig. S68). ICP-MS and XPS analyses showed that the total content of metals reached 17.99 wt % (Fe: 1.2 wt %; Co: 0.81 wt %, Ni: 0.76 wt %, Cu: 0.93 wt %, Zn: 0.67 wt %, Pt: 3.84 wt %, Pd: 4.62 wt %, Ir: 3.16 wt %).

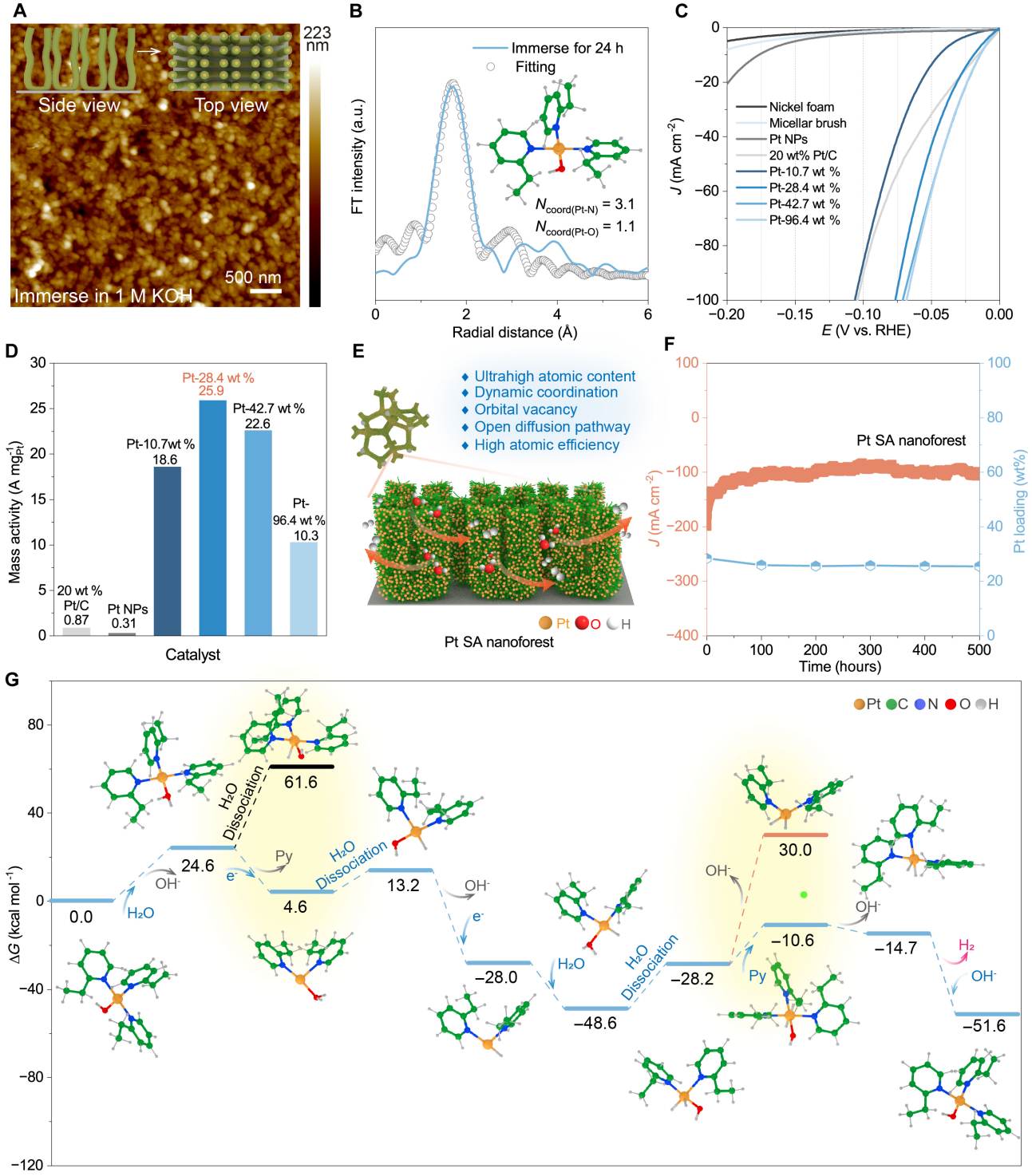

Fig. 5. Electrochemical performance of the Pt SA nanoforest as an HER catalyst. (**A**) Fluid AFM height image of the Pt SA nanoforest in a solution of 1.0 M KOH. Inset illustrates the side and top views of the erect nanoforest. (**B**) FT-EXAFS spectra of the Pt SA nanoforest after immersion in a solution of 1.0 M KOH, and corresponding EXAFS fitting curve for *R*-space. N_{coord} denotes the average number of ligands coordinated with a Pt atom. (**C**) Linear sweep voltammetry (LSV) curves of naked nickel foam and nickel foams coated with micellar brush, 20 wt % Pt/C on nickel foam, Pt NPs on nickel foam, and micellar brushes loaded with the lower-content Pt SA nanoforest (10.7 wt % Pt), Pt SA nanoforest (28.4 wt % Pt), Pt cluster–decorated micellar brush (42.7 wt % Pt), and Pt nanoparticle–decorated micellar brush (96.4 wt % Pt), with iR correction in an aqueous solution of KOH (1.0 M) at a scan rate of 5 mV s^{-1}. (**D**) Mass activities of Pt in 20 wt % Pt/C on nickel foam, Pt NPs on nickel foam, and the lower-content Pt SA nanoforest (10.7 wt %), Pt SA nanoforest (28.4 wt % Pt), Pt cluster–decorated micellar brush (42.7 wt % Pt) and Pt nanoparticle–decorated micellar brush (96.4 wt % Pt). (**E**) Schematic illustration of the catalytic environment of the Pt SA nanoforest. (**F**) Chronopotentiometry measurements of Pt SA nanoforest–decorated nickel foam recorded at −0.92 V versus RHE for a continuous period of 500 hours and loading of Pt SA during the continuous test. (**G**) Possible intermediates and relative energy diagram for the HER catalyzed by the Pt SA nanoforest. Voltage is set to 2.0 V, the pH is set to 14.0, and the concentration of OH^- is set to 1.0 M. The free energies involved refer to the overall energy of each stage.

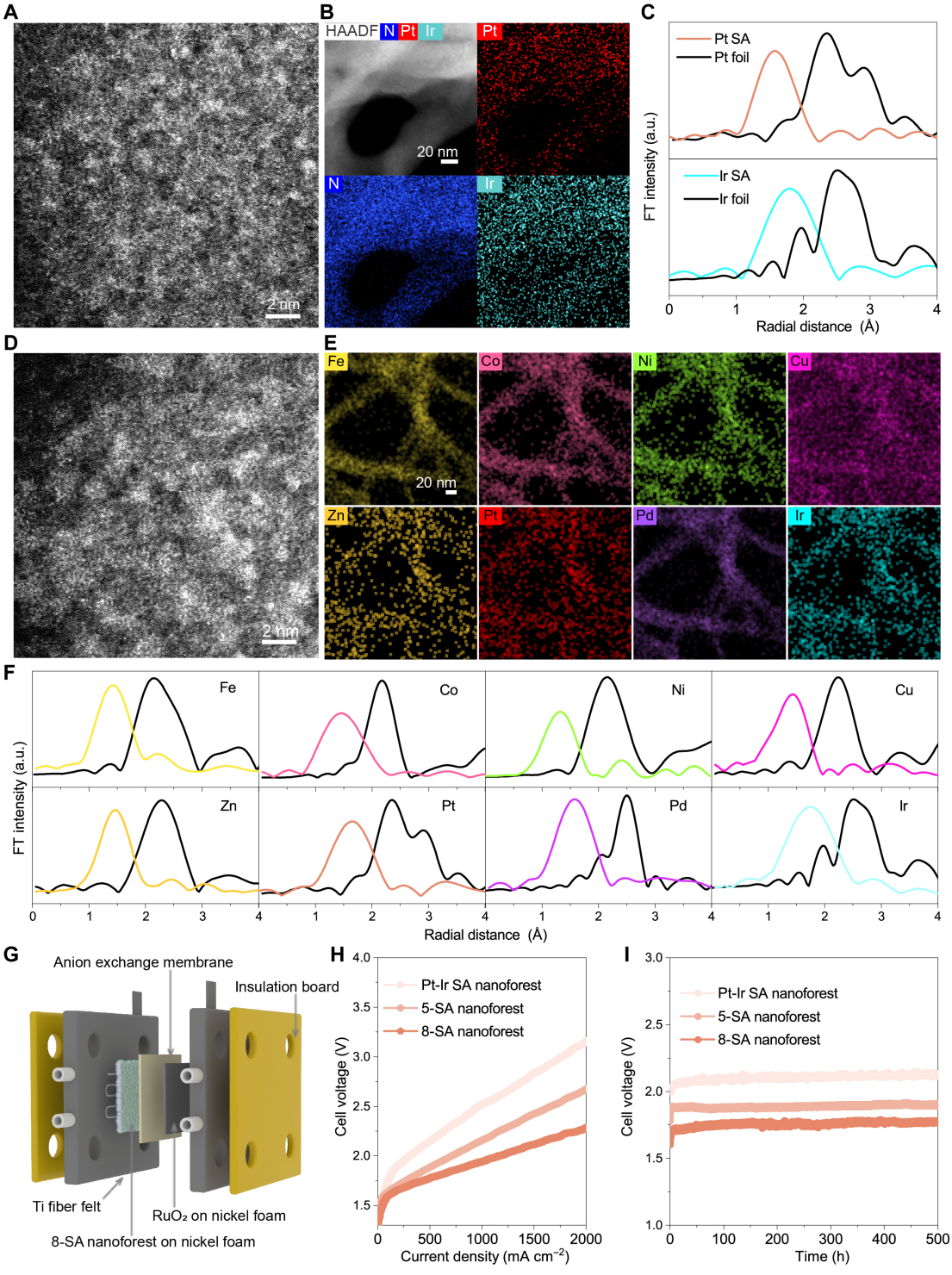

Fig. 6. Fabrication of nanoforest containing multiple SAs for AEM. (**A**) AC-ADF-STEM images, (**B**) HAADF-STEM image and the corresponding element mapping of the Pt-Ir SA nanoforest. (**C**) FT-EXAFS spectra of the Pt-Ir SA nanoforest, with reference to Pt and Ir foils. (**D** to **F**) AC-ADF-STEM image (D), the corresponding element mapping (E), and FT-EXAFS spectra (F) of the 8-SA nanoforest and the corresponding reference metal foils (black lines). (**G**) Schematic illustration of the AEM electrolyzer device. (**H**) *I-V* curves of the AEM electrolyzer using Pt-Ir SA, 5-SA, and 8-SA nanoforests as the cathodic catalyst and commercial RuO_2 as the anodic catalyst under 60°C. (**I**) Chronopotentiometry tests of Pt-Ir SA, 5-SA, and 8-SA nanoforest catalysts at a current density of 500 mA cm^{-2} for 500 hours at 60°C in a solution of 1.0 M KOH. h, hours.

To investigate the potential application of a multi-SA nanoforest catalyst for water electrolysis, we fabricated an AEM water electrolyzer using the multi-SA nanoforest as the cathode catalyst and commercial RuO_2 as the anode catalyst, separated by an AEM (Fig. 6G). The AEM water electrolyzer device performance was evaluated at 60°C under ambient pressure, using a solution of KOH (1.0 M) as the electrolyte. The current-voltage (*I-V*) curve of the 8-SA nanoforest revealed a voltage of 1.77 V at a current density of 500 mA cm^{-2} and a voltage of 1.94 V at a current density of 1.0 A cm^{-2}, which were considerably better than the Pt-Ir SA nanoforest (2.18 V, 2.5 V) or the 5-SA nanoforest (1.86 V, 2.1 V, Fig. 6H and fig. S70). Although it is not clear so far, such improved water electrolysis activity may be attributed to the synergy of various metal SA in the catalytic reactions. In addition, we also evaluated the stability of the Pt-Ir, 5-SA, and 8-SA nanoforests at a current density of 500 mA cm^{-2} for 500 hours at 60°C (Fig. 6I). No obvious cell voltage increase was observed for these metal SA nanoforests. After the test, only 0.2% metal loss was found for the 8-SA nanoforest, indicating an ultrahigh stability of the atomically dispersed metal catalysts supported by the micellar brush.

DISCUSSION

In summary, we have developed a micellar brush–derived soft nanoforest system to immobilize SAs on conventional electrodes. Nanoforests of 33 types of individual SAs were fabricated with high atomic contents of 8.3 to 40.9 wt %. The resulting Pt SA nanoforest was highly solvated in the electrolyte and thus provides an open diffusion pathway. The dynamic coordination between the metals and the pyridine groups allowed the substitution of one hydroxyl group before the electrochemical reaction. Hence, the Pt SA nanoforest on nickel foam revealed high mass activity but considerably low overpotential, Tafel slope, and charge-transfer resistance for electrochemical hydrogen evolution. Moreover, the micellar brush support also allowed the simultaneous immobilization of two to eight types of SAs, and the 8-SA nanoforest revealed a low cell voltage of 1.77 V at 500 mA cm^{-2} for water electrolysis by an AEM electrolyzer. The forest-like hierarchically open structure of the micellar brushes, combined with the presence of abundant pyridine groups and the derived chelation effect, plays a crucial role in anchoring an ultrahigh amount of diverse SAs under mild conditions. Such forest-like environment also improves the utilization efficiency of SAs and favors the catalytic reactions due to the well-solvated and highly dispersed forest-like structure, as well as the dynamic coordination. Further work is currently conducting on modulating the feature of SAs by introducing other coordinative groups in the nanoforest and exploring the synergistic effects by spatial deposition of various SAs using segmental micellar brushes.

MATERIALS AND METHODS

Polymer synthesis

PFS-*b*-P2VP block copolymers were synthesized via sequential living anionic polymerization as previously reported (*23*).

Characterization

Scanning electron microscopy (SEM) images were obtained on a JSM-7800F Prime microscope. Transmission electron microscopy (TEM) and HAADF-STEM images were measured on a FEI TALOS F200X microscope with an acceleration voltage of 200 kV. AC-ADF-STEM images were obtained on a Hitachi HF 5000 microscope operated at 200 kV and equipped with a spherical aberration corrector. XPS data were collected on a Thermo Fisher Scientific–Nexsa spectroscope with monochromatic Al K radiation. ICP-MS data were collected on the NexION2000 Flexar20 HPLC system. X-ray absorption spectroscopy (XAS) measurements were conducted on the BL14W1 and BL13SSW beamlines of Shanghai Synchrotron Radiation Facility (SSRF), China.

Preparation of PFS-*b*-P2VP micelle seeds

Polydisperse long cylindrical micelles were prepared by dissolving the PFS_{44}-*b*-$P2VP_{526}$ polymer in isopropanol (0.5 mg ml^{-1}) by stirring at 60°C for ca. 30 min followed by an aging process at room temperature for 1 day. The long cylindrical micelles were subsequently fragmentized by sonication with a probe ultrasonic processor (80 W, Ningbo Scientz Biotechnology Co. Ltd) at 0°C in an ice-water bath for 45 min and allowed to age for 1 day.

Immobilization of PFS-*b*-P2VP micelle seeds on nickel foam

A piece of nickel foam (1 cm × 1 cm) was sonicated in acetone and water for 6 hours, respectively, and dried under a gentle stream of nitrogen. The nickel foam was subjected to O_2 plasma treatment for 30 s, and then immersed in a solution of the PFS_{44}-*b*-$P2VP_{526}$ micelle seeds (150 μl, 0.5 mg ml^{-1} in isopropanol) for 30 min, and dried under a gentle stream of nitrogen. The resulting nickel foam was aged at room temperature for 1 day and rinsed with isopropanol several times to remove the poorly immobilized micelle seeds and lastly dried under nitrogen flow.

Growth of the PFS-*b*-P2VP micellar brush on nickel foam

The PFS_{44}-*b*-$P2VP_{526}$ micelle seed–coated nickel foam was immersed in 2 ml of isopropanol. Subsequently, 10 μl of a solution of the PFS_{27}-*b*-$P2VP_{356}$ unimers (10 mg ml^{-1} in THF) was added. The sample was shaken for 30 min using a shaker and allowed to age for 1 day. Then, the resulting sample was rinsed with isopropanol several times and dried under nitrogen flow.

Decoration of SAs in micellar brush

The PFS-*b*-P2VP micellar brush–coated nickel foam was immersed in 10 ml of a mixture of 1:1 (v/v) isopropanol/deionized water and then 50 μl of an aqueous solution of Na_2PtCl_4 (10 mg ml^{-1}) was added. After 30 min, the resulting sample was washed with deionized water and isopropanol, and lastly dried under nitrogen flow. The synthesis of other SA-decorated micellar brushes followed the same immersion process and the metal precursors are specified in table S3. For the synthesis of nanoforests containing multiple SAs, various metal precursors were simultaneously added. For the synthesis of lower-content atomically dispersed Pt, Pt clusters and Pt NPs, 25, 100, and 200 μl of a solution of Na_2PtCl_4 (10 mg ml^{-1}) were added.

Growth of the PFS-*b*-P2VP micellar brush on GO sheets and decoration of SAs

GO sheets were prepared by the Hummers method (*70*). The resulting GO sheets were dispersed in isopropanol (0.5 mg ml^{-1}) followed by sonication for 2 hours. Subsequently, 100 μl of the solution of GO sheets was mixed with 1 ml of isopropanol and then 150 μl of a solution of the PFS_{44}-*b*-$P2VP_{526}$ micelle seeds (0.5 mg ml^{-1} in isopropanol) was added to the system. The mixture was stirred for 1 day at room temperature. The poorly immobilized micelle seeds were removed by three sedimentation/re-dispersal cycles. The PFS-*b*-P2VP

micelle seed–coated GO sheets were dispersed in 4 ml of isopropanol and then 10 μl of a solution of the PFS_{27}-*b*-$P2VP_{356}$ unimers (10 mg ml^{-1} in THF) was added. The mixture was stirred for 1 day at room temperature. The resulting sample was purified by three sedimentation/re-dispersal cycles. Then, the solution was mixed with 10 ml of a mixture of 1:1 (v/v) isopropanol/deionized water, followed by the addition of 50 μl of an aqueous solution of $NaAuCl_4$ or $AgNO_3$ (10 mg ml^{-1}). After stirring for 30 min, the final sample was washed with isopropanol and lastly dried under vacuum environment.

Electrochemical hydrogen evolution

All the electrochemical measurements were evaluated using a three-electrode system on an electrochemical workstation (CH Instrument 760E). The as-synthesized samples, Ag/AgCl electrode, and platinum foil were used as working, reference, and counter electrodes, respectively. An aqueous solution of KOH (1.0 M) was used as the electrolyte. All the calculated potential was referenced to a reversible hydrogen electrode (RHE) according to the following equation: E (versus RHE) = E (versus Ag/AgCl) + E^0 (Ag/AgCl) + 0.059 × pH. LSV tests were conducted at a scan rate of 5 mV s^{-1} and the results were collected with iR compensation. Electrochemical impedance spectra (EIS) were recorded at a potential of −0.1 V (versus RHE) in a frequency range of 0.01 to 100,000 Hz. Regarding the control experiments involving the commercial Pt/C catalyst, 1 mg of 20 wt % Pt/C was dissolved in a mixture of 950 μl of ethanol and 50 μl of Nafion solution (5 wt %) to form a homogeneous catalyst ink. Then, 200 μl of the catalyst ink was loaded on a nickel foam (1 cm × 1 cm) and lastly dried at 60°C for 2 hours in an oven. Mass activity of dispersed SAs was calculated by the following formula

$$\text{Mass current density (Pt)} = \frac{J_{\text{Pt}} \times A_{\text{nickel foam}}}{m_{\text{Pt}}}$$

where J_{Pt} is the current density of the Pt SA nanoforest, $A_{\text{nickel foam}}$ is the area of nickel foam as electrode, and m_{Pt} is the loading of Pt SAs.

Hydrogen-underpotential deposition (H_{UPD}) was used to measure the ECSA by recording the cyclic voltammetry (CV) profile (*71*–*73*). The potential range scanned was 0.05 to 1.2 V (versus RHE) in N_2-saturated 0.1 M $HClO_4$. The working electrode was initially scanned for 30 cycles at a scan rate of 80 mV s^{-1} to activate the catalyst surface, followed by 2 cycles at 50 mV s^{-1} to calculate the ECSA. The ECSA (m^2 g^{-1}) was calculated using the following formula: $\text{ECSA} = \frac{Q_H}{C \times m_{\text{PNF}}}$, where Q_H (mC cm^{-2}) is the integrated CV curve from ~0.05 to 0.4 V (versus RHE) from the hydrogen desorption peak area, C is the hydrogen adsorption constant (0.21 mC cm^{-2}), and m_{PNF} (mg_{Pt} cm^{-2}) is the Pt loading mass.

The H_2 TOF value was calculated using the following formula (*74*): $\text{TOF per site} = \frac{\text{the number of total hydrogen turnover}}{\text{the number of surface site}}$. The number of total hydrogen turnover was calculated from the current density at 50 mV by the following formula

$$\text{Number of } H_2 = \left(j\frac{\text{mA}}{\text{cm}^2}\right)\left(\frac{1\frac{\text{C}}{\text{s}}}{1000\text{ mA}}\right)\left(\frac{1\text{ mol } e^-}{96{,}485\text{ C}}\right)\left(\frac{1\text{ mol } H_2}{2\text{ mol } e^-}\right)$$
$$\left(\frac{6.02\times10^{23}\text{molecules } H_2}{1\text{ mol } H_2}\right) = 3.12\times10^{15}\ \frac{\frac{H_2}{\text{s}}}{\text{cm}^2}\ \text{per}\ \frac{\text{mA}}{\text{cm}^2}$$

The density of Pt is 21.45 g cm^{-3} and, hence, the molar volume of Pt is 9.09 cm^3mol−1. Number of surface sites = $\left(\frac{6.02\times10^{23}\text{ atoms}}{1\text{ mol}} \times \frac{1\text{ mol}}{9.09\text{ cm}^3}\right)^{\frac{2}{3}}$ = $1.637\times10^{15}\ \frac{\text{atoms}}{\text{cm}^2}$. Thus, $\text{TOF} = \frac{\left(3.12\times10^{15}\ \frac{\frac{H_2}{\text{s}}}{\text{cm}^2}\ \text{per}\ \frac{\text{mA}}{\text{cm}^2}\right)\times|j|}{1.637\times10^{15}\ \frac{\text{atoms}}{\text{cm}^2}\times A}$, where A is ECSA (cm^2).

AEM water electrolysis test

The AEM performance was tested in a self-made cell with a two-electrode system. The AEM cell consists of two titanium plates as anode and cathode, respectively, with serpentine flow channels. The AEM (HoAM Grion 1204, Hangzhou LvHe Environmental Technology Co. Ltd.) was soaked in a solution of 1.0 M KOH for more than 24 hours before use. The metal SA nanoforest on nickel foam (1 cm × 1 cm) was used as the HER cathode. Commercial RuO_2 (ca. 5 mg ml^{-1} in ethanol) was mixed with Nafion binder and subsequently dropped on a piece of nickel foam (1 cm × 1 cm), which was as the OER anode. The cell was then circulated with 1.0 M KOH aqueous solution at 60 ml min^{-1}. *I*-*V* curves were collected at 60°C under ambient pressure. The stability of the AEM electrolyzer was evaluated by measuring the chronopotentiometry at 500 mA cm^{-2} for 500 hours at 60°C under ambient pressure.

Electrochemical CO_2 reduction

Ten milligrams of the powder of Au or Ag SA nanoforest–coated GO sheets was dispersed in 1 ml of a mixture of water, ethanol, and Nafion solution (5 wt %) (5:4:1, v/v/v) by sonication to form a homogeneous catalyst ink. Then, 800 μl of the ink was dropped in a 2 cm × 2 cm gas diffusion electrode (GDE), which was used as the working electrode. The mass loading of the SA nanoforest–coated GO sheets was 2.0 ± 0.1 mg cm^{-2}. The CO_2 reduction performance was evaluated using a flow cell equipped with the above GDE on an electrochemical workstation (Autolab PGSTAT 302 N). The flow rate of CO_2 and electrolyte solution was controlled at 30 and 5 ml min^{-1}, respectively. An aqueous solution of KOH (1.0 M) was used as the electrolyte. The Ag/AgCl electrode was used as the reference electrode, and a Ti mesh with an Ir black loading of 2 mg cm^{-2} was used as the counter electrode. All the calculated potential was referenced to RHE and corrected by iR compensation. The gas products were analyzed using gas chromatography (GC), and the liquid products were characterized using proton nuclear magnetic resonance (^{1}H NMR) spectroscopy. Faradic efficiency was calculated via the following equation

$$\text{FE} = \frac{Q_{\text{CO}}}{Q_{\text{total}}} = \frac{N \times n \times F}{Q_{\text{total}}}$$

where FE is Faradic efficiency, N is the number of electrons transferred, n is the number of moles for a given product, F is Faraday's constant (96,485 C mol^{-1}), and Q_{total} denotes all the charge consumed throughout the electrolysis process.

EXAFS curve fitting and data analysis

The EXAFS data were processed by using the ATHENA module implemented in the IFEFFIT software package (*75*). Quantitative curve fittings were conducted for the Fourier-transformed k^2-weighted $\chi(k)$ in the *R*-space with a Fourier transform *k*-space range of 2.3 to 12 $Å^{-1}$ using the module ARTEMIS 4 in the IFEFFIT software package. The phase shift $\Phi(k)$ and backscattering amplitude $F(k)$ were calculated by FEFF 8.0 code. All curve fittings were conducted with

a fixed amplitude reduction factor (S_0^2) of 0.65 to 1.00. The parameters coordinated number (CN), interatomic distance (R), the Debye-Waller factor (σ^2), and the edge-energy shift (ΔE_0) were opened to be varied. The common adjustable parameters ΔE_0 and σ^2 were used to reduce the number of free parameters. The error in the overall fits was determined by using the R factor (R_f). Good fits require an R factor < 0.02.

DFT calculations

DFT calculations were carried out using the Gaussian 16 program (*76*). Geometrical optimization calculations were carried out at the PBE0-D3(BJ) (*77*, *78*)/def2-SVP (*79*) level with the SMD continuum solvent model (*80*) for water without any symmetry assumptions unless otherwise stated. Harmonic vibration frequency calculations were performed at the same level for verifying the resulting geometries as local minima (with all the frequencies real). To improve the relative energy, we further performed the single point calculations on the optimized geometries at the PBE0-D3(BJ) (*77*, *78*)/def2-QZVP (*79*) level with the SMD continuum solvent model for water. 2-Ethylpyridine was used to represent the pyridyl polymer P2VP for simplicity during the calculation. For the calculation of HER mechanism, SHE is set to 4.44 V and voltage V_{set} is set to 2.0 V, the pH value is set to 14, and the concentration of OH^- is set to 1.0 M.

Supplementary Materials

This PDF file includes:

Supplementary Text
Figs. S1 to S71
Tables S1 to S11

REFERENCES AND NOTES

1. C. A. Witham, W. Huang, C.-K. Tsung, J. N. Kuhn, G. A. Somorjai, F. D. Toste, Converting homogeneous to heterogeneous in electrophilic catalysis using monodisperse metal nanoparticles. *Nat. Chem.* **2**, 36–41 (2010).
2. H. Yang, X. Wang, Q. Liu, A. Huang, X. Zhang, Y. Yu, Z. Zhuang, G. Li, Y. Li, Q. Peng, X. Chen, H. Xiao, C. Chen, Heterogeneous iridium single-atom molecular-like catalysis for epoxidation of ethylene. *J. Am. Chem. Soc.* **145**, 6658–6670 (2023).
3. M. K. Samantaray, V. D'Elia, E. Pump, L. Falivene, M. Harb, S. Ould Chikh, L. Cavallo, J.-M. Basset, The comparison between single atom catalysis and surface organometallic catalysis. *Chem. Rev.* **120**, 734–813 (2020).
4. C. Zhu, S. Fu, Q. Shi, D. Du, Y. Lin, Single-atom electrocatalysts. *Angew. Chem. Int. Ed. Engl.* **56**, 13944–13960 (2017).
5. P. N. Duchesne, Z. Y. Li, C. P. Deming, V. Fung, X. Zhao, J. Yuan, T. Regier, A. Aldalbahi, Z. Almarhoon, S. Chen, D.-e. Jiang, N. Zheng, P. Zhang, Golden single-atomic-site platinum electrocatalysts. *Nat. Mater.* **17**, 1033–1039 (2018).
6. L. Liu, A. Corma, Metal catalysts for heterogeneous catalysis: From single atoms to nanoclusters and nanoparticles. *Chem. Rev.* **118**, 4981–5079 (2018).
7. S. Ye, F. Luo, Q. Zhang, P. Zhang, T. Xu, Q. Wang, D. He, L. Guo, Y. Zhang, C. He, X. Ouyang, M. Gu, J. Liu, X. Sun, Highly stable single Pt atomic sites anchored on aniline-stacked graphene for hydrogen evolution reaction. *Energ. Environ. Sci.* **12**, 1000–1007 (2019).
8. Y. Wang, H. Su, Y. He, L. Li, S. Zhu, H. Shen, P. Xie, X. Fu, G. Zhou, C. Feng, D. Zhao, F. Xiao, X. Zhu, Y. Zeng, M. Shao, S. Chen, G. Wu, J. Zeng, C. Wang, Advanced electrocatalysts with single-metal-atom active sites. *Chem. Rev.* **120**, 12217–12314 (2020).
9. D. Cao, Z. Zhang, Y. Cui, R. Zhang, L. Zhang, J. Zeng, D. Cheng, One-step approach for constructing high-density single-atom catalysts toward overall water splitting at industrial current densities. *Angew. Chem. Int. Ed. Engl.* **62**, e202214259 (2023).
10. Y. Qu, Z. Li, W. Chen, Y. Lin, T. Yuan, Z. Yang, C. Zhao, J. Wang, C. Zhao, X. Wang, F. Zhou, Z. Zhuang, Y. Wu, Y. Li, Direct transformation of bulk copper into copper single sites via emitting and trapping of atoms. *Nat. Catal.* **1**, 781–786 (2018).
11. X. Sun, S. R. Dawson, T. E. Parmentier, G. Malta, T. E. Davies, Q. He, L. Lu, D. J. Morgan, N. Carthey, P. Johnston, S. A. Kondrat, S. J. Freakley, C. J. Kiely, G. J. Hutchings, Facile synthesis of precious-metal single-site catalysts using organic solvents. *Nat. Chem.* **12**, 560–567 (2020).
12. J. Xi, H. S. Jung, Y. Xu, F. Xiao, J. W. Bae, S. Wang, Synthesis strategies, catalytic applications, and performance regulation of single-atom catalysts. *Adv. Funct. Mater.* **31**, 2008318 (2021).
13. Y. Zhou, F. Wei, H. Qi, Y. Chai, L. Cao, J. Lin, Q. Wan, X. Liu, Y. Xing, S. Lin, A. Wang, X. Wang, T. Zhang, Peripheral-nitrogen effects on the Ru_1 centre for highly efficient propane dehydrogenation. *Nat. Catal.* **5**, 1145–1156 (2022).
14. B. Qiao, A. Wang, X. Yang, L. F. Allard, Z. Jiang, Y. Cui, J. Liu, J. Li, T. Zhang, Single-atom catalysis of CO oxidation using Pt_1/FeO_x. *Nat. Chem.* **3**, 634–641 (2011).
15. S. Yang, J. Kim, Y. J. Tak, A. Soon, H. Lee, Single-atom catalyst of platinum supported on titanium nitride for selective electrochemical reactions. *Angew. Chem. Int. Ed. Engl.* **55**, 2058–2062 (2016).
16. J. Jones, H. Xiong, A. T. DeLaRiva, E. J. Peterson, H. Pham, S. R. Challa, G. Qi, S. Oh, M. H. Wiebenga, X. I. Pereira Hernández, Y. Wang, A. K. Datye, Thermally stable single-atom platinum-on-ceria catalysts via atom trapping. *Science* **353**, 150–154 (2016).
17. H. Li, L. Wang, Y. Dai, Z. Pu, Z. Lao, Y. Chen, M. Wang, X. Zheng, J. Zhu, W. Zhang, R. Si, C. Ma, J. Zeng, Synergetic interaction between neighbouring platinum monomers in CO_2 hydrogenation. *Nat. Nanotechnol.* **13**, 411–417 (2018).
18. X.-P. Yin, H.-J. Wang, S.-F. Tang, X.-L. Lu, M. Shu, R. Si, T.-B. Lu, Engineering the coordination environment of single-atom platinum anchored on graphdiyne for optimizing electrocatalytic hydrogen evolution. *Angew. Chem. Int. Ed. Engl.* **57**, 9382–9386 (2018).
19. X. Zeng, J. Shui, X. Liu, Q. Liu, Y. Li, J. Shang, L. Zheng, R. Yu, Single-atom to single-atom grafting of Pt_1 onto Fe–N_4 center: Pt_1@Fe–N–C multifunctional electrocatalyst with significantly enhanced properties. *Adv. Energy Mater.* **8**, 1701345 (2018).
20. Y. Sun, Y. Zang, W. Tian, X. Yu, J. Qi, L. Chen, X. Liu, H. Qiu, Plasma-induced large-area N,Pt-doping and phase engineering of MoS_2 nanosheets for alkaline hydrogen evolution. *Energy Environ. Sci.* **15**, 1201–1210 (2022).
21. X. Han, X. Ling, Y. Wang, T. Ma, C. Zhong, W. Hu, Y. Deng, Generation of nanoparticle, atomic-cluster, and single-atom cobalt catalysts from zeolitic imidazole frameworks by spatial isolation and their use in zinc-air batteries. *Angew. Chem. Int. Ed. Engl.* **58**, 5359–5364 (2019).
22. R. Qin, K. Liu, Q. Wu, N. Zheng, Surface coordination chemistry of atomically dispersed metal catalysts. *Chem. Rev.* **120**, 11810–11899 (2020).
23. J. Cai, C. Li, N. Kong, Y. Lu, G. Lin, X. Wang, Y. Yao, I. Manners, H. Qiu, Tailored multifunctional micellar brushes via crystallization-driven growth from a surface. *Science* **366**, 1095–1098 (2019).
24. G. Lin, J. Cai, Y. Sun, Y. Cui, Q. Liu, I. Manners, H. Qiu, Capillary-bound dense micelle brush supports for continuous flow catalysis. *Angew. Chem. Int. Ed. Engl.* **60**, 24637–24643 (2021).
25. S. Wang, W. Xie, P. Wu, G. Lin, Y. Cui, J. Tao, G. Zeng, Y. Deng, H. Qiu, Soft nanobrush-directed multifunctional MOF nanoarrays. *Nat. Commun.* **13**, 6673 (2022).
26. X. Hai, S. Xi, S. Mitchell, K. Harrath, H. Xu, D. F. Akl, D. Kong, J. Li, Z. Li, T. Sun, H. Yang, Y. Cui, C. Su, X. Zhao, J. Li, J. Pérez-Ramírez, J. Lu, Scalable two-step annealing method for preparing ultra-high-density single-atom catalyst libraries. *Nat. Nanotechnol.* **17**, 174–181 (2022).
27. L. Han, H. Cheng, W. Liu, H. Li, P. Ou, R. Lin, H.-T. Wang, C.-W. Pao, A. R. Head, C.-H. Wang, X. Tong, C.-J. Sun, W.-F. Pong, J. Luo, J.-C. Zheng, H. L. Xin, A single-atom library for guided monometallic and concentration-complex multimetallic designs. *Nat. Mater.* **21**, 681–688 (2022).
28. T. Li, J. Liu, Y. Song, F. Wang, Photochemical solid-phase synthesis of platinum single atoms on nitrogen-doped carbon with high loading as bifunctional catalysts for hydrogen evolution and oxygen reduction reactions. *ACS Catal.* **8**, 8450–8458 (2018).
29. L. Zhang, L. Han, H. Liu, X. Liu, J. Luo, Potential-cycling synthesis of single platinum atoms for efficient hydrogen evolution in neutral media. *Angew. Chem. Int. Ed. Engl.* **56**, 13694–13698 (2017).
30. J. Zhu, L. Cai, X. Yin, Z. Wang, L. Zhang, H. Ma, Y. Ke, Y. Du, S. Xi, A. T. S. Wee, Y. Chai, W. Zhang, Enhanced electrocatalytic hydrogen evolution activity in single-atom Pt-decorated VS_2 nanosheets. *ACS Nano* **14**, 5600–5608 (2020).
31. C. Li, Z. Chen, H. Yi, Y. Cao, L. Du, Y. Hu, F. Kong, R. Kramer Campen, Y. Gao, C. Du, G. Yin, I. Y. Zhang, Y. Tong, Polyvinylpyrrolidone-coordinated single-site platinum catalyst exhibits high activity for hydrogen evolution reaction. *Angew. Chem. Int. Ed. Engl.* **59**, 15902–15907 (2020).
32. H. Jin, S. Sultan, M. Ha, J. N. Tiwari, M. G. Kim, K. S. Kim, Simple and scalable mechanochemical synthesis of noble metal catalysts with single atoms toward highly efficient hydrogen evolution. *Adv. Funct. Mater.* **30**, 2000531 (2020).
33. Q. Cheng, C. Hu, G. Wang, Z. Zou, H. Yang, L. Dai, Carbon-defect-driven electroless deposition of pt atomic clusters for highly efficient hydrogen evolution. *J. Am. Chem. Soc.* **142**, 5594–5601 (2020).
34. L. Zhang, Y. Jia, H. Liu, L. Zhuang, X. Yan, C. Lang, X. Wang, D. Yang, K. Huang, S. Feng, X. Yao, Charge polarization from atomic metals on adjacent graphitic layers for enhancing the hydrogen evolution reaction. *Angew. Chem. Int. Ed. Engl.* **58**, 9404–9408 (2019).
35. J. Park, S. Lee, H.-E. Kim, A. Cho, S. Kim, Y. Ye, J. W. Han, H. Lee, J. H. Jang, J. Lee, Investigation of the support effect in atomically dispersed Pt on WO_{3-x} for utilization of Pt in the hydrogen evolution reaction. *Angew. Chem. Int. Ed. Engl.* **58**, 16038–16042 (2019).

36. D. Liu, X. Li, S. Chen, H. Yan, C. Wang, C. Wu, Y. A. Haleem, S. Duan, J. Lu, B. Ge, P. M. Ajayan, Y. Luo, J. Jiang, L. Song, Atomically dispersed platinum supported on curved carbon supports for efficient electrocatalytic hydrogen evolution. *Nat. Energy* **4**, 512–518 (2019).
37. K. Jiang, B. Liu, M. Luo, S. Ning, M. Peng, Y. Zhao, Y.-R. Lu, T.-S. Chan, F. M. F. de Groot, Y. Tan, Single platinum atoms embedded in nanoporous cobalt selenide as electrocatalyst for accelerating hydrogen evolution reaction. *Nat. Commun.* **10**, 1743 (2019).
38. J. Ji, Y. Zhang, L. Tang, C. Liu, X. Gao, M. Sun, J. Zheng, M. Ling, C. Liang, Z. Lin, Platinum single-atom and cluster anchored on functionalized MWCNTs with ultrahigh mass efficiency for electrocatalytic hydrogen evolution. *Nano Energy* **63**, 103849 (2019).
39. L. Zhang, R. Long, Y. Zhang, D. Duan, Y. Xiong, Y. Zhang, Y. Bi, Direct observation of dynamic bond evolution in single-atom Pt/C_3N_4 catalysts. *Angew. Chem. Int. Ed. Engl.* **59**, 6224–6229 (2020).
40. X.-H. Jiang, L.-S. Zhang, H.-Y. Liu, D.-S. Wu, F.-Y. Wu, L. Tian, L.-L. Liu, J.-P. Zou, S.-L. Luo, B.-B. Chen, Silver single atom in carbon nitride catalyst for highly efficient photocatalytic hydrogen evolution. *Angew. Chem. Int. Ed. Engl.* **59**, 23112–23116 (2020).
41. A. S. Mahadevi, G. N. Sastry, Cation-pi interaction: Its role and relevance in chemistry, biology, and material science. *Chem. Rev.* **113**, 2100–2138 (2013).
42. H. Zhang, K. Li, X. Guo, L. Zhang, D. Cao, D. Cheng, Rational regulation of the defect density in platinum nanocrystals for highly efficient hydrogen evolution reaction. *Small* **20**, e2306694 (2024).
43. Q. Liang, W. Li, L. Xie, Y. He, B. Qiu, H. Zeng, S. Zhou, J. Zeng, T. Liu, M. Yan, K. Liang, O. Terasaki, L. Jiang, B. Kong, General synergistic capture-bonding superassembly of atomically dispersed catalysts on micropore-vacancy frameworks. *Nano Lett.* **22**, 2889–2897 (2022).
44. X. Wang, L. Bai, J. Lu, X. Zhang, D. Liu, H. Yang, J. Wang, P. K. Chu, S. Ramakrishna, X.-F. Yu, Rapid activation of platinum with black phosphorus for efficient hydrogen evolution. *Angew. Chem. Int. Ed. Engl.* **58**, 19060–19066 (2019).
45. X.-K. Wan, H. B. Wu, B. Y. Guan, D. Luan, X. W. D. Lou, Confining sub-nanometer Pt clusters in hollow mesoporous carbon spheres for boosting hydrogen evolution activity. *Adv. Mater.* **32**, 1901349 (2020).
46. Z. Zhao, H. Liu, W. Gao, W. Xue, Z. Liu, J. Huang, X. Pan, Y. Huang, Surface-engineered PtNi-O nanostructure with record-high performance for electrocatalytic hydrogen evolution reaction. *J. Am. Chem. Soc.* **140**, 9046–9050 (2018).
47. H. Huang, L. Fu, W. Kong, H. Ma, X. Zhang, J. Cai, S. Wang, Z. Xie, S. Xie, Equilibrated Ptlr/IrO_x atomic heterojunctions on ultrafine 1D nanowires enable superior dual-electrocatalysis for overall water splitting. *Small* **18**, 2201333 (2022).
48. D. S. Baek, G. Y. Jung, B. Seo, J. C. Kim, H.-W. Lee, T. J. Shin, H. Y. Jeong, S. K. Kwak, S. H. Joo, Ordered mesoporous metastable alpha-MoC_{1-x} with enhanced water dissociation capability for boosting alkaline hydrogen evolution activity. *Adv. Funct. Mater.* **29**, 1901217 (2019).
49. M. Lao, K. Rui, G. Zhao, P. Cui, X. Zheng, S. X. Dou, W. Sun, Platinum/nickel bicarbonate heterostructures towards accelerated hydrogen evolution under alkaline conditions. *Angew. Chem. Int. Ed. Engl.* **58**, 5432–5437 (2019).
50. S. Niu, J. Yang, H. Qi, Y. Su, Z. Wang, J. Qiu, A. Wang, T. Zhang, Single-atom Pt promoted Mo_2C for electrochemical hydrogen evolution reaction. *J. Energy Chem.* **57**, 371–377 (2021).
51. X. Peng, H. Bao, J. Sun, Z. Mao, Y. Qiu, Z. Mo, L. Zhuo, S. Zhang, J. Luo, X. Liu, Heteroatom coordination induces electric field polarization of single Pt sites to promote hydrogen evolution activity. *Nanoscale* **13**, 7134–7139 (2021).
52. W. Yang, P. Cheng, Z. Li, Y. Lin, M. Li, J. Zi, H. Shi, G. Li, Z. Lian, H. Li, Tuning the cobalt–platinum alloy regulating single-atom platinum for highly efficient hydrogen evolution reaction. *Adv. Funct. Mater.* **32**, 2205920 (2022).
53. K. L. Zhou, Z. Wang, C. B. Han, X. Ke, C. Wang, Y. Jin, Q. Zhang, J. Liu, H. Wang, H. Yan, Platinum single-atom catalyst coupled with transition metal/metal oxide heterostructure for accelerating alkaline hydrogen evolution reaction. *Nat. Commun.* **12**, 3783 (2021).
54. B. Fan, H. Wang, X. Han, Y. Deng, W. Hu, Single atoms (Pt, Ir and Rh) anchored on activated NiCo LDH for alkaline hydrogen evolution reaction. *Chem. Commun.* **58**, 8254–8257 (2022).
55. J. Wei, K. Xiao, Y. Chen, X.-P. Guo, B. Huang, Z.-Q. Liu, In situ precise anchoring of Pt single atoms in spinel $Mn_3O_4$for a highly efficient hydrogen evolution reaction. *Energy Environ. Sci.* **15**, 4592–4600 (2022).
56. W. Yu, H. Huang, Y. Qin, D. Zhang, Y. Zhang, K. Liu, Y. Zhang, J. Lai, L. Wang, The synergistic effect of pyrrolic-n and pyridinic-n with Pt under strong metal-support interaction to achieve high-performance alkaline hydrogen evolution. *Adv. Energy Mater.* **12**, 2200110 (2022).
57. C. Zhang, X. Liang, R. Xu, C. Dai, B. Wu, G. Yu, B. Chen, X. Wang, N. Liu, H_2 in situ inducing strategy on Pt surface segregation over low Pt doped $PtNi_5$ nanoalloy with superhigh alkaline HER activity. *Adv. Funct. Mater.* **31**, 2008298 (2021).
58. D. A. Salvatore, D. M. Weekes, J. He, K. E. Dettelbach, Y. C. Li, T. E. Mallouk, C. P. Berlinguette, Electrolysis of gaseous CO_2 to CO in a flow cell with a bipolar membrane. *ACS Energy Lett.* **3**, 149–154 (2018).
59. C.-T. Dinh, F. P. García de Arquer, D. Sinton, E. H. Sargent, High Rate, selective, and stable electroreduction of CO_2 to CO in basic and neutral media. *ACS Energy Lett.* **3**, 2835–2840 (2018).
60. Y. E. Kim, B. Kim, W. Lee, Y. N. Ko, M. H. Youn, S. K. Jeong, K. T. Park, J. Oh, Highly tunable syngas production by electrocatalytic reduction of CO_2 using Ag/TiO_2 catalysts. *Chem. Eng. J.* **413**, 127448 (2021).
61. Y. Xu, J. P. Edwards, S. Liu, R. K. Miao, J. E. Huang, C. M. Gabardo, C. P. O'Brien, J. Li, E. H. Sargent, D. Sinton, Self-cleaning CO_2 reduction systems: Unsteady electrochemical forcing enables stability. *ACS Energy Lett.* **6**, 809–815 (2021).
62. J. Chen, Z. Wang, H. Lee, J. Mao, C. A. Grimes, C. Liu, M. Zhang, Z. Lu, Y. Chen, S.-P. Feng, Efficient electroreduction of CO_2 to CO by Ag-decorated S-doped $g\text{-}C_3N_4$/CNT nanocomposites at industrial scale current density. *Mater. Today Phys.* **12**, 100176 (2020).
63. Z. Qi, M. M. Biener, A. R. Kashi, S. Hunegnaw, A. Leung, S. Ma, Z. Huo, K. P. Kuhl, J. Biener, Electrochemical CO_2 to CO reduction at high current densities using a nanoporous gold catalyst. *Mater. Res. Lett.* **9**, 99–104 (2021).
64. S. Verma, Y. Hamasaki, C. Kim, W. Huang, S. Lu, H.-R. M. Jhong, A. A. Gewirth, T. Fujigaya, N. Nakashima, P. J. A. Kenis, Insights into the low overpotential electroreduction of CO_2 to CO on a supported gold catalyst in an alkaline flow electrolyzer. *ACS Energy Lett.* **3**, 193–198 (2018).
65. R. Shi, J. Guo, X. Zhang, G. I. N. Waterhouse, Z. Han, Y. Zhao, L. Shang, C. Zhou, L. Jiang, T. Zhang, Efficient wettability-controlled electroreduction of CO_2 to CO at Au/C interfaces. *Nat. Commun.* **11**, 3028 (2020).
66. H.-R. M. Jhong, C. E. Tornow, C. Kim, S. Verma, J. L. Oberst, P. S. Anderson, A. A. Gewirth, T. Fujigaya, N. Nakashima, P. J. A. Kenis, Gold nanoparticles on polymer-wrapped carbon nanotubes: An efficient and selective catalyst for the electroreduction of CO_2. *ChemPhysChem* **18**, 3274–3279 (2017).
67. J. Chen, H. Li, C. Fan, Q. Meng, Y. Tang, X. Qiu, G. Fu, T. Ma, Dual single-atomic $Ni\text{-}N_4$ and $Fe\text{-}N_4$ sites constructing janus hollow graphene for selective oxygen electrocatalysis. *Adv. Mater.* **32**, 2003134 (2020).
68. A. Han, X. Wang, K. Tang, Z. Zhang, C. Ye, K. Kong, H. Hu, L. Zheng, P. Jiang, C. Zhao, Q. Zhang, D. Wang, Y. Li, An adjacent atomic platinum site enables single-atom iron with high oxygen reduction reaction performance. *Angew. Chem. Int. Ed. Engl.* **60**, 19262–19271 (2021).
69. P. Rao, Y. Deng, W. Fan, J. Luo, P. Deng, J. Li, Y. Shen, X. Tian, Movable type printing method to synthesize high-entropy single-atom catalysts. *Nat. Commun.* **13**, 5071 (2022).
70. W. S. Hummers Jr., R. E. Offeman, Preparation of graphitic oxide. *J. Am. Chem. Soc.* **80**, –1339 (1958).
71. K. Xu, L. Liang, T. Li, M. Bao, Z. Yu, J. Wang, S. M. Thalluri, F. Lin, Q. Liu, Z. Cui, S. Song, L. Liu, $Pt_{1.8}Pd_{0.2}$CuGa intermetallic nanocatalysts with enhanced methanol oxidation performance for efficient hybrid seawater electrolysis. *Adv. Mater.* **36**, 2403792 (2024).
72. S. T. Dix, S. Lu, S. Linic, Critical practices in rigorously assessing the inherent activity of nanoparticle electrocatalysts. *ACS Catal.* **10**, 10735–10741 (2020).
73. D. Chen, Q. Tao, L. W. Liao, S. X. Liu, Y. X. Chen, S. Ye, Determining the active surface area for various platinum electrodes. *Electrocatalysis* **2**, 207–219 (2011).
74. A. Wang, G. Long, J. Chen, X. An, T. Yao, C. Li, Electrocatalysts with highly dispersed cerium in nickel matrix for hydrogen evolution in alkaline electrolyte. *Adv. Energy Mater.* **14**, 2400647 (2024).
75. A. L. Ankudinov, B. Ravel, J. J. Rehr, S. D. Conradson, Real-space multiple-scattering calculation and interpretation of x-ray-absorption near-edge structure. *Phys. Rev. B* **58**, 7565–7576 (1998).
76. M. J. Frisch, G. W. Trucks, H. B. Schlegel, G. E. Scuseria, M. A. Robb, J. R. Cheeseman, G. Scalmani, V. Barone, B. Mennucci, G. A. Petersson, H. Nakatsuji, X. Li, M. Caricato, A. V. Marenich, J. Bloino, B. G. Janesko, R. Gomperts, B. Mennucci, H. P. Hratchian, J. V. Ortiz, A. F. Izmaylov, J. L. Sonnenberg, D. Williams-Young, F. Ding, F. Lipparini, F. Egidi, J. Goings, B. Peng, A. Petrone, T. Henderson, D. Ranasinghe, V. G. Zakrzewski, J. Gao, N. Rega, G. Zheng, W. Liang, M. Hada, M. Ehara, K. Toyota, R. Fukuda, J. Hasegawa, M. Ishida, T. Nakajima, Y. Honda, O. Kitao, H. Nakai, T. Vreven, K. Throssell, J. A. Montgomery Jr., J. E. Peralta, F. Ogliaro, M. J. Bearpark, J. J. Heyd, E. N. Brothers, K. N. Kudin, V. N. Staroverov, T. A. Keith, R. Kobayashi, J. Normand, K. Raghavachari, A. P. Rendell, J. C. Burant, S. S. Iyengar, J. Tomasi, M. Cossi, J. M. Millam, M. Klene, C. Adamo, R. Cammi, J. W. Ochterski, R. L. Martin, K. Morokuma, O. Farkas, J. B. Foresman, D. J. Fox, Gaussian 16, Revision A.03 (Gaussian, Inc., 2016).
77. C. Adamo, V. Barone, Toward reliable density functional methods without adjustable parameters: The PBE0 model. *J. Chem. Phys.* **110**, 6158–6170 (1999).
78. S. Grimme, J. Antony, S. Ehrlich, H. Krieg, A consistent and accurate ab initio parametrization of density functional dispersion correction (DFT-D) for the 94 elements H-Pu. *J. Chem. Phys.* **132**, 154104 (2010).
79. F. Weigend, R. Ahlrichs, Balanced basis sets of split valence, triple zeta valence and quadruple zeta valence quality for H to Rn: Design and assessment of accuracy. *Phys. Chem. Chem. Phys.* **7**, 3297–3305 (2005).

80. A. V. Marenich, C. J. Cramer, D. G. Truhlar, Universal solvation model based on solute electron density and on a continuum model of the solvent defined by the bulk dielectric constant and atomic surface tensions. *J. Phys. Chem. B* **113**, 6378–6396 (2009).

Acknowledgments

Funding: This work was financially supported by the National Key R&D Program of China (2020YFA0908100 and 2021YFA1500300), the National Natural Science Foundation of China (22425203, 22075180, and 22072090), the Innovation Program of Shanghai Municipal Education Commission (202101070002E00084), the Science and Technology Commission of Shanghai Municipality (21XD1421900), Science Foundation of Zhejiang Sci-Tech University grant 22062026-Y, Zhejiang Provincial Natural Science Foundation of China grant LY23B040003, the China Postdoctoral Science Foundation (2023M732190), and the Fundamental Research Funds for the Central Universities (YG2023ZD29 and YG2023ZD07). This work was also supported by BL14W, BL13SSW, and the User Experiment Assist System of SSRF.

Author contributions: Y.S. and H.Q. conceived the project. Y.S. performed the synthetic experiments and analyzed the samples with assistance from Y.Z. and L.Y. G.L. prepared the polymer samples and performed the AFM test. C.S. conducted the theoretical calculation. B.H., L.C., and X.L. conducted the aberration-corrected scanning transmission electron microscopy measurements. Z.L. and L.L. conducted the XAS measurements. Y.S. and H.Q. analyzed the data and prepared the manuscript with input from all the other authors. The project was supervised by H.Q. **Competing interests:** The authors declare that they have no competing interests. **Data and materials availability:** All data needed to evaluate the conclusions in the paper are present in the paper and/or the Supplementary Materials.

Submitted 7 May 2024
Accepted 10 December 2024
Published 15 January 2025
10.1126/sciadv.adq2948